Rotational stabilization of resistive wall modes in ITER advanced tokamak scenarios[a]

L. J. Zheng,[b] M. T. Kotschenreuther, and J. W. Van Dam

Institute for Fusion Studies, University of Texas at Austin, Austin, Texas 78712, USA

Rotational stabilization of $n=1$ resistive wall modes in ITER advanced scenarios [K. Ikeda, Nucl. Fusion **47** (2007)] is investigated, where n is the toroidal mode number. In particular, we present numerical results for the ITER strongly reversed shear case, in comparison to the weakly reversed shear case. The rotation frequency is assumed to be modestly low. Our investigation employs the adaptive eigenfunction independent solution-kinetic (AEGIS-K) code [L. J. Zheng *et al.*, "AEGIS-K code for linear kinetic analysis of toroidally axisymmetric plasma stability," J. Comput. Phys. (to be published)], which provides a fully kinetic (nonhybrid) and self-consistent (nonperturbative) description. AEGIS-K includes wave-particle resonances, shear Alfvén continuum damping, trapped particle effects, and parallel electric effects, but not finite Larmor radius effects. In the case without rotation and kinetic effects included, we find that the strongly reversed shear configuration is more favorable for perfectly conducting wall stabilization of resistive wall modes, in that it has a higher conducting wall beta limit than the weakly reversed shear case. With sufficient rotation, the strongly reversed shear case can also achieve a higher beta limit for completely suppressing the resistive wall modes. However, the marginal rotation frequency required for complete resistive wall mode stabilization in the strongly reversed shear case is about twice as high as that required for the weakly reversed shear case. © *2010 American Institute of Physics*. [doi:10.1063/1.3318267]

I. INTRODUCTION

One of the important goals of ITER (Ref. 1) is to demonstrate the so-called advanced scenarios: i.e., the reactor scale steady-state operation for tokamaks. However, such steady-state high beta fusion plasmas with reversed magnetic shear are likely to be unstable to long-wavelength external kink modes. The external kink modes can in principle be stabilized by a perfectly conducting wall, allowing the stable beta value to increase above the no-wall stability limit. However, if the wall has finite conductivity, the external kink modes are converted to the so-called resistive wall modes (RWMs), which grow slowly on the resistive wall time.[2] Therefore, the stability of RWMs becomes a major concern for ITER advanced scenarios.[3]

Considerable theoretical and numerical efforts have been made to determine the stabilization regimes for RWMs. It has been shown previously that the kinetic and Alfvén resonances can play significant roles in stabilizing the RWMs.[4–7] However, a satisfactory systematic investigation of RWMs remains a challenging issue. On one hand, one needs to formulate the problem in a nonperturbed and nonkinetic-fluid-hybrid manner theoretically. On the other hand, one needs to develop a numerical scheme with high radial resolution in order to study the continuum damping and its coupling to the kinetic one computationally. The present paper reports our effort in resolving this challenging issue.

On the theoretical side, we have extended the conventional gyrokinetic theory so that it can maintain consistency of ordering and recover full magnetohydrodynamics (MHD).

This was reported in Ref. 8. The success in recovering full MHD with our newly derived gyrokinetic theory now allows the possibility to consistently study the stability of RWMs in a nonhybrid manner. Kinetic effects have also been investigated with so-called hybrid approach. When finite Larmor radius (FLR) effects are neglected, our nonhybrid model should be equivalent to properly formulated hybrid approaches. Our approach, moreover, has the advantage of systematically including all relevant kinetic effects.

On the numerical side, we have implemented a nonperturbative formalism and developed a radially adaptive numerical scheme by extending our MHD adaptive eigenfunction independent solution (AEGIS) shooting code (Ref. 9) to a kinetic version AEGIS-kinetic (AEGIS-K).[10] The radially adaptive numerical scheme seems to be unavoidable. One can estimate the requirement for the number of radial grid points in a grid-based numerical scheme, using an ideal MHD code such as GATO.[11] In general, GATO works with 300 radial grid points for a reasonable numerical convergence. In a kinetic description, however, the matrices become complex and non-Hermitian. It is hard to have good numerical convergence with 300 radial grid points. To resolve the singular layer physics in a kinetic description, one needs more than double the size of 300 radial grid points. This sets a hard obstacle to overcome for the grid-based method. In contrast, increasing the radial resolution in our AEGIS-K numerical scheme does not lead to an increase in matrix size. Due to its adaptive numerical scheme, AEGIS-K does not have the radial convergence problem. This shows the numerical advantage of the AEGIS-K formalism.

To make this challenging issue tractable, we limit ourselves in this work to a consideration of the case with mod-

estly low rotation frequency. In this frequency regime, the FLR effects can be neglected, especially the precessional drift resonance effect.[7] Low rotation case is of interest for ITER.

The paper is arranged as follows. In Sec. II, the AEGIS-K code and its theoretical formalism are outlined. In Sec. III, the numerical results are presented. In Sec. IV, we give discussion and conclusions.

II. AEGIS-K CODE AND ITS THEORETICAL FORMALISM

In order to have a nonhybrid numerical analysis of MHD modes, one needs to develop a kinetic theory that recovers MHD-like equation structure. As described in detail in Ref. 8, we found that conventional gyrokinetics can only achieve a partial recovery of the MHD-like equation structure. There are four main reasons for conventional gyrokinetic theory to lose the MHD fluid root: (1) the equilibrium distribution function has not been solved to a sufficient order. Note that the Pfirsch–Schlüter current results from the equilibrium distribution function of the first order, as shown in the neoclassical transport theory. Therefore, the conventional approach of only using the lowest order equilibrium distribution function (e.g., Maxwellian distribution function) leads the Pfirsch–Schlüter current effect not to be included. (2) Solving only the gyrophase-independent part of the gyrokinetic equation also contributes to the exclusion of the Pfirsch–Schlüter current effect. This is because the Pfirsch–Schlüter current effect is present in the term $\mathbf{v} \times \delta\mathbf{B} \cdot \nabla_v F$, which depends on the gyrophase. Here, $\mathbf{v}$ is the particle velocity, $\delta\mathbf{B}$ denotes the perturbed magnetic field, and F is the equilibrium distribution function. We have used boldface to represent vectors. One needs to solve for full Fourier harmonics of the perturbed distribution function in gyrophase in order to retain the Pfirsch–Schlüter current effect. (3) Coupling between the gyrophase-independent and dependent parts of the distribution function through the term $\dot{\alpha}_1 \partial \delta f / \partial \alpha$ has not been taken into account. Here, δf is the perturbed distribution function and α is the gyrophase, with the subscript "1" denoting the first order in the small Larmor radius expansion and the dot representing the time derivative along the unperturbed particle orbit. (4) A correction to the next-order gyrophase expression needs to be made: $\dot{\alpha}_1 = \mathbf{v} \cdot \nabla \alpha + (1/\Omega)\mathbf{v} \times \mathbf{e}_b \cdot \nabla \Omega$. Only with corrections (1) and (2) included can the $\mathbf{J} \times \delta\mathbf{B}$ term, where $\mathbf{J}$ is the equilibrium current, be recovered and the MHD equations perpendicular to the magnetic field be fully reproduced. Also, only with corrections (3) and (4) can the parallel MHD equation of motion be retrieved in the proper limit.

Inclusion of corrections (1)–(4) also results in the recovery of the FLR effects that are missing in the conventional gyrokinetic formalism. The usual description of the FLR effects through the Bessel functions J_0 and J_1 is incomplete. From Ref. 8, one can see that the FLR effects even in the second order is much more complicated than those given by J_0 and J_1. Therefore, in pursuing the kinetic analysis of the stability of MHD modes, we will advance our numerical

work step by step. In our current work we will neglect the FLR effects by choosing a suitable rotation frequency regime.

We therefore focus on the case with modestly low rotation frequency, smaller than the ion transit frequency but larger than the ion diamagnetic frequency ω_{*i}. In this limit, the basic set of equations is composed of the perpendicular Ampére's law

$$-\rho_m \hat{\omega}^2 \boldsymbol{\xi} = \delta\mathbf{J} \times \mathbf{B} + \mathbf{J} \times \delta\mathbf{B} - \nabla \delta P_c$$
$$-\nabla_\perp \int d^3 v (m_\rho \mu B) \delta f_{0i}(\mathbf{x}), \qquad (1)$$

the gyrophase-independent part of the gyrokinetic equation

$$\mathbf{v}_\parallel \cdot \nabla \delta f_{0i}(\mathbf{X}) - i\hat{\omega} \delta f_{0i}(\mathbf{X})$$
$$= i\hat{\omega} \frac{m_\rho}{T_i} \mu B F_0 \nabla_\perp \cdot \boldsymbol{\xi} + i\hat{\omega} \frac{m_\rho}{T_i}(\mu B - v_\parallel^2) F_0 \boldsymbol{\kappa} \cdot \boldsymbol{\xi}$$
$$- i\hat{\omega} \frac{Ze_i}{T_i} F_0 \delta\varphi, \qquad (2)$$

and the quasineutrality condition

$$\delta\varphi = -\frac{1}{1 + Z\tau} \frac{T_e}{Ze_i} \frac{1}{n_0} \int d^3 v \, \delta f_{0i}. \qquad (3)$$

Here, $\boldsymbol{\xi}$ is the perpendicular field line displacement, $\mathbf{B}$ denotes the equilibrium magnetic field, $\delta\mathbf{B} = \nabla \times \boldsymbol{\xi} \times \mathbf{B}$, $\delta\mathbf{J} = \nabla \times \delta\mathbf{B}$, P represents the equilibrium pressure, $\delta P_c = -\boldsymbol{\xi} \cdot \nabla P$ is the perturbed pressure of convective part, ρ_m is the mass density, m_ρ denotes the mass, e_i is the ion charge, Z is the charge number, n_0 is the ion density, $\mu = v_\perp^2 / 2B$ is the magnetic moment, T represents the temperature, $\tau = T_i/T_e$ with subscripts i and e representing, respectively, the ion and electron species, $\boldsymbol{\kappa}$ represents the field line curvature, $\delta\varphi$ specifies the parallel electric field effect, δf_{0i} denotes the gyrophase averaged distribution function for ion spices, F_0 is the Maxwellian distribution function, and the subscripts $\perp$ and $\parallel$ represent, respectively, the perpendicular and the parallel components of the equilibrium magnetic field line. Due to the low mode frequency, we have assumed the electron response to be adiabatic. Here, we note that, without the parallel electric field effect [the last term on the right hand side of Eq. (2)], Eq. (2) agrees with the nongyrokinetic formulation in Ref. 12 derived by using the method of integration along the unperturbed particle orbit.

In our ordering scheme, the rotation frequency is much lower than the ion acoustic frequency. We can then include the rotational effects through a Doppler shift in our formalism, i.e., by replacing the mode frequency ω with $\hat{\omega} \equiv \omega + n\Omega$ in Eqs. (1)–(3), where $\Omega(\psi)$ is the rotation frequency and ψ is the poloidal magnetic flux. In actuality, rotation effects enter into the problem in three categories—that is, not only through the Doppler shift but also via centrifugal force and Coriolis force. For the case when the rotation speed is much less than the ion thermal speed, however, it can be shown that the rotational effects of centrifugal force and Coriolis force are negligibly small.[13] Consequently, we can keep only the rotational effect from the Doppler shift. Note
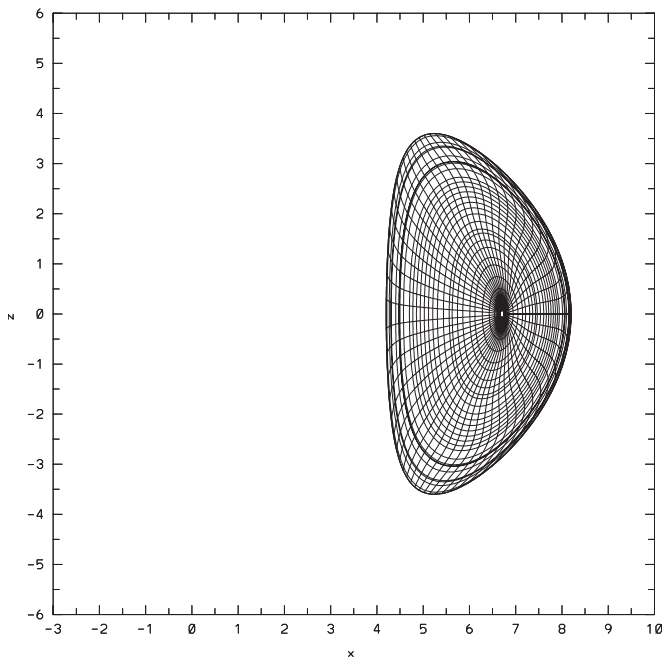
FIG. 1. Cross section of the ITER advanced tokamak configuration with strongly reversed shear. The poloidal coordinate shown here is the Hamada coordinate. The packed radial grids for output of eigenfunctions are shown in diluted grid density.

FIG. 2. Typical safety factor profiles for strongly (solid) and weakly (dashed) reversed shear cases, respectively.

that the effect of the radial dependence of the Doppler shift (or the rotation shear effect) has been included in our formulation (see Ref. 10).

In our set of equations, Eqs. (1)–(3), the wave-particle resonances, the shear Alfvén continuum damping, the trapped particle effect, and the parallel electric effects are all taken into account. The precessional drift resonance as studied in Ref. 7 has not been included in our consideration. We postpone this work for future investigation, since it is a more complex target. Considering the precessional drift resonance alone is insufficient for ordering consistency. First, since $\langle \omega_d \rangle / \omega_{*i}$ is of order of the inverse aspect ratio a/R, inclusion of the $\langle \omega_d \rangle$ effect also needs to take into account the ω_{*i} effect together with the FLR effects of order $k_\perp^2 \rho_i^2$, which, as pointed out in Ref. 8, is much more complicated than that predicted in the conventional theory. Here, $k_\perp$ is the perpendicular wave number and ρ_i is the ion gyroradius. Second, one also needs to include finite orbit size effects through the magnetic drift velocity in the minor radius direction in considering the precessional drift effect.

To implement our newly derived set of equations, Eqs. (1)–(3), we extend our existing AEGIS code[9] to the kinetic AEGIS-K code.[10] In our formalism, Fourier decomposition is employed in the poloidal direction. In the radial direction, decomposition using the independent solutions is used. The independent solutions are then obtained by adaptive numerical shooting. There is a difficulty to apply this method for global eigenmode calculation, related to the numerical pollution of the large solution associated with independent solutions at the singular surfaces. We developed a multiple-region matching method to overcome this difficulty. In ideal MHD stability calculations, we have demonstrated the suc-
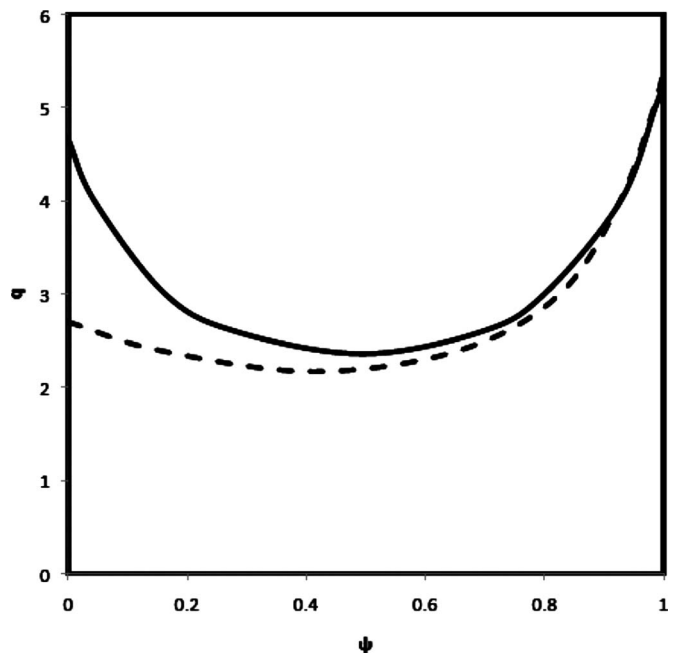
cess of this method in the AEGIS formalism.[9] We also find that this method works equally well for the kinetic problem.[10] Since the AEGIS formalism is based on the adaptive numerical scheme, we are able to resolve the coupling between the kinetic and the shear Alfvén resonances.

III. NUMERICAL RESULTS

We used our AEGIS-K code to study $n=1$ RWMs in ITER advanced tokamak scenarios, where n is the toroidal mode number. We focused on the strongly reversed shear case in this paper, with comparison made to the weakly reversed shear case that we investigated previously in Ref. 14. The numerical equilibrium was generated by the TOQ code (an MHD equilibrium code developed at General Atomics, San Diego, CA).[15] The typical parameters for strongly reversed shear case (for $\beta_N = 3.4$) were as follows: $q_0 = 4.67$, $q_a = 5.25$, $q_{\min} = 2.36$, $q_{95} = 4.26$, elongation $\kappa_a = 1.8$, and triangularity $\delta_a = 0.48$. Here, q_0, q_a, $q_{\min}$, and q_{95} are, respectively, the safety factor values at the magnetic axis, the plasma edge, the q minimum, and the 95% radial flux surface. The rotation profile is specified as $\Omega(1 - \psi^2)$. We assume a conformal wall in the present calculation and assume the equilibrium to be up-down symmetric. A typical plasma cross section is given in Fig. 1. The typical safety factor profiles both for strongly and weakly reversed shear cases are shown in Fig. 2. As in Ref. 3, we define the strongly reversed shear case as the case with $q_0 - q_{\min} > 2$.

We first present the RWM stability diagram for the cases without kinetic and rotation effects as a baseline reference for the subsequent kinetic analyses. We use the MHD code AEGIS to determine this diagram. The AEGIS code is in complete agreement with GATO (Ref. 11) for ideal MHD computations.[8] The solid and dashed curves in Fig. 3 show the ideal MHD stability conditions for the strongly and
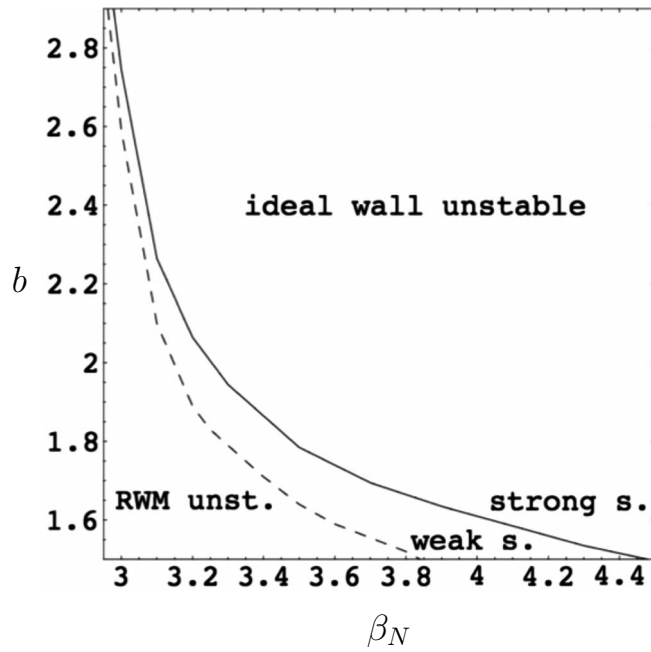
FIG. 3. Critical wall position b for ideal MHD RWMs vs beta normal β_N without rotation for strongly (solid) and weakly (dashed) reversed shear cases.
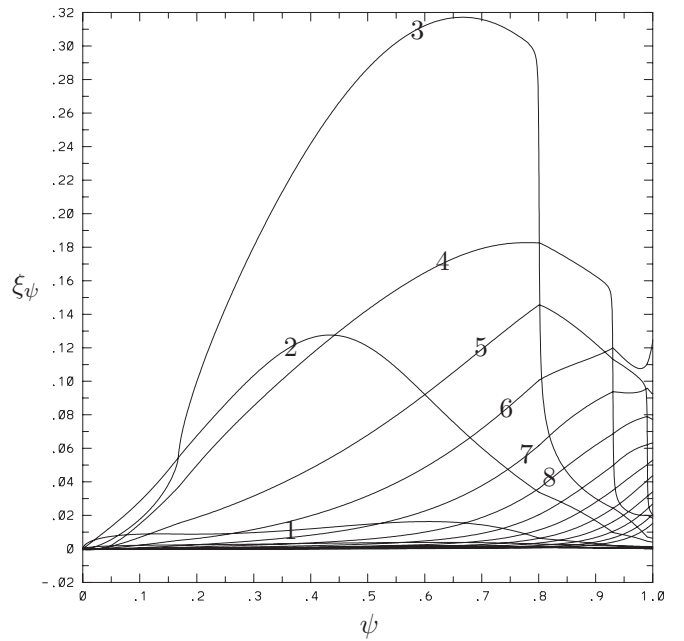

FIG. 4. Fourier components of the radial field line displacement vs radial coordinate ψ for typical unstable RWMs without rotation, as computed by AEGIS for the strongly reversed shear case with beta normal $\beta_N=3.4$. The poloidal mode numbers are tagged to the corresponding curves.

weakly reversed shear cases. The stability conditions are given in terms of the critical wall position b (normalized by the minor radius) versus the beta normal value $\beta_N \equiv \beta(I/aB_0)^{-1}$, where β is the ratio of the plasma energy to the magnetic energy, I is the tokamak toroidal current, a is the minor radius, and B_0 denotes the magnetic field at the magnetic axis. The dashed curve for the weakly reversed shear case is reproduced from Ref. 14. Figure 3 shows that the strongly reversed shear case has higher critical wall position than the weakly reversed shear case. This indicates that strongly reversed shear is favorable for perfectly conducting wall stabilization. In particular, for ITER wall position $b=1.5$, the critical beta value for the weakly reversed shear case is $\beta_N=4.48$, whereas for the weakly reversed shear case it is $\beta_N=3.94$. This indicates that strongly reversed shear improves the confinement considerably for perfectly conducting wall stabilization of RWMs. The unstable regions are above the curves. As usual, the unstable RWMs are recovered in the perfectly conducting wall stabilization region. Nevertheless, we note that the no-wall limits do not vary much between strongly and weakly reversed shear cases. Based on our equilibrium cases explored so far, we are still not certain whether this is just a coincidence. This will be further investigated in the future. A typical ideal MHD eigenmode for the strongly reversed shear case is shown in Fig. 4.

We used the AEGIS-K code to study the effects of rotation and kinetic effects on the RWMs in the ITER strongly reversed shear case. We find that RWMs can be stabilized by rotation and kinetic effects. A typical unstable kinetic eigenmode in the strongly reversed shear case is given in Fig. 5 for beta normal $\beta_N=3.4$ and normalized rotation frequency $\Omega=0.015$. Note that the rotation frequency Ω is normalized by the Alfvén speed $\sqrt{B^2/(\mu_0\rho_m R^2 q^2)}$ at the magnetic axis with q included. Here, R is the major radius and μ_0 is the

magnetic permeability. One of the advantages of the AEGIS-K code is that it preserves the ideal MHD roots. This can be seen from a comparison between Fig. 4 and Fig. 5(a).

Using AEGIS-K, we can study the dependence of RWM stability on the beta value. For this purpose, we consider a series of numerical equilibria with beta normal values ranging from the no-wall limit $\beta_N^{\text{no wall}}=2.95$ to the ideal-wall limit $\beta_N^{\text{ideal wall}}=4.48$ for fixed wall position $b=1.5$. Figure 6 shows the RWM growth rate versus beta normal for a given wall position $b=1.5$ for the strongly reversed shear case for various rotation frequencies. The left and right vertical dotted lines in Fig. 6 represent the no-wall and perfectly conducting wall beta limits, respectively. RWMs are unstable for the beta value between these two dotted lines for the case without rotation and kinetic effects included. The case of $\Omega=0.03$ was also computed, and full stabilization was obtained with this rotation frequency. Figure 6 shows that the growth rate generally decreases as the rotation frequency increases. This shows that rotation gives rise to stabilization of RWMs in the kinetic description.

Similar to the weakly reversed shear case reported in Ref. 14, we find that the rotational and kinetic stabilization first appears near the ideal-wall stability limit as the rotation frequency increases. One can explain this behavior with the energy picture introduced in Ref. 5. Expressed in terms of no-wall and ideal-wall energy integrals δW_∞ and δW_b,[2] the RWM growth rate can be written as follows:

$$\gamma \sim -\frac{\delta W_\infty^r \delta W_b^r + \delta W_\infty^i \delta W_b^i}{|\delta W_b^r|^2 + |\delta W_b^i|^2}, \tag{4}$$

where the superscripts r and i represent the real and imaginary parts, respectively. Without rotation and kinetic effects ($\delta W_\infty^i = \delta W_b^i = 0$), the RWM growth rate tends to infinity at the
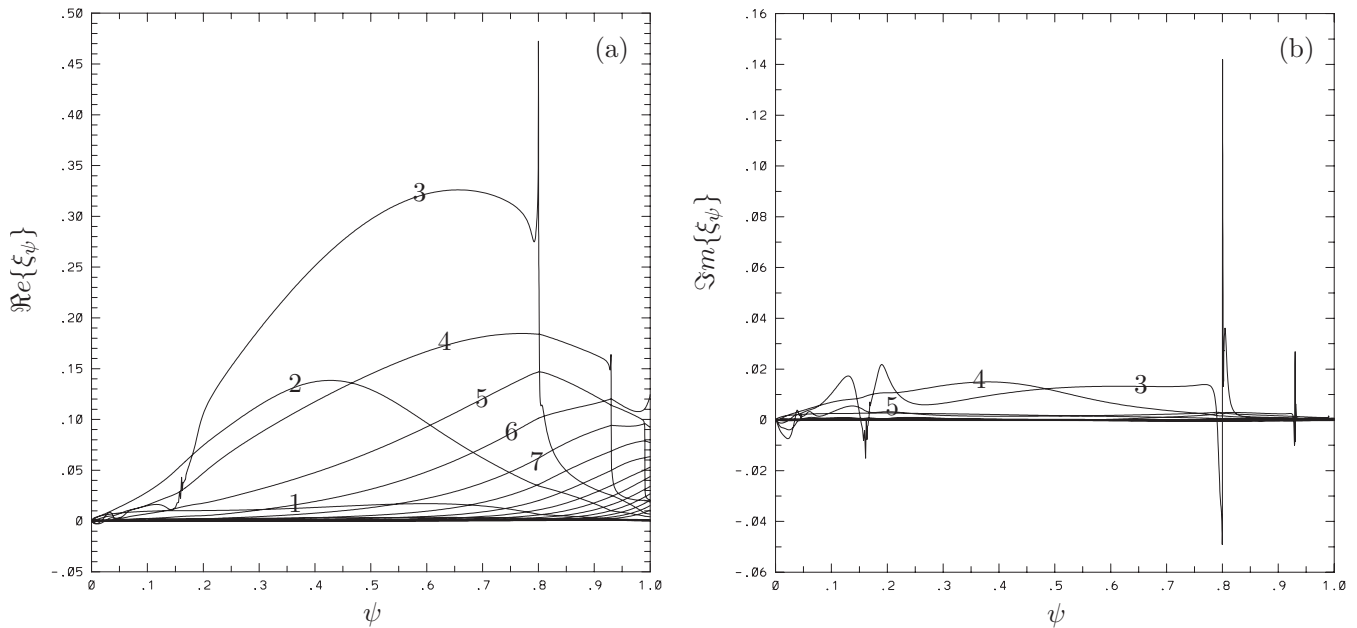
FIG. 5. Real (a) and imaginary (b) parts of the Fourier components of the radial field line displacement vs radial coordinate ψ for an unstable RWM in the presence of rotation and kinetic effects, with equilibrium parameters: $\beta_N = 3.4$, $\Omega = 0.015$, and $b = 1.5$. The poloidal mode numbers are tagged to the corresponding curves.

ideal-wall limit $\delta W_b^r = 0$ (dashed curve in Fig. 6). In the presence of rotation and kinetic effects ($\delta W_\infty^i \delta W_b^i \neq 0$), the numerator of Eq. (4) shows that $\delta W_b^r = 0$ is also the point that is most easily to be stabilized by the rotation and kinetic effects through the resonance-induced imaginary part of the energy $\delta W_\infty^i \delta W_b^i$. This explanation applies only for the cases with sufficiently high rotation. If rotation is too low, the kinetic stabilization effects are not strong enough to overcome the RWM development. Consequently, the large RWM growth rate causes the thermal particles to become nonresonant with the modes, so that no stabilization window opens up near the ideal-wall limit. In Figs. 6 and 7, we have not plotted curves with insufficient rotation, because their behavior is similar to the curve with zero rotation.

To compare with the weakly reversed shear case, we reproduce the figure for the RWM growth rate versus beta normal given in Fig. 7 of Ref. 14. In contrast to Ref. 14, here we use the actual beta normal as the horizontal coordinate, instead of the beta parameter C_β. We first point out that our normalization of the rotation frequency by the Alfvén frequency at the magnetic axis includes the safety factor at the magnetic axis, q_0. As shown in Fig. 2, the safety factor at the magnetic axis for the strongly reversed shear case is larger than that for the weakly reversed shear case. Therefore, we need to exclude the q_0 normalization factor to compare the results in Figs. 6 and 7. As reported above, full stabilization of the RWM in the strongly reversed shear case occurs for $\Omega = 0.03$. Excluding the q_0 factor, we find that this value reduces to 0.006. As shown in Ref. 14, full stabilization of the RWM in the weakly reversed shear case occurs for $\Omega = 0.0075$. Excluding the q_0 factor, we find that this value becomes 0.003. This shows that the rotation frequency required for full stabilization in the strongly reversed shear case is about twice that in the weakly reversed shear case.

Nevertheless, note that the achievable beta value with full rotation stabilization in the strongly reversed shear case ($\beta_N = 4.48$) is considerably larger than that in the weakly reversed shear case. From a comparison between the eigenmodes for the strongly reversed shear case in Fig. 5 and those for the weakly reversed shear case in Ref. 14, one can see that there are two additional resonance surfaces ($m = 3$ and 4) on the reversed shear side in the strongly reversed
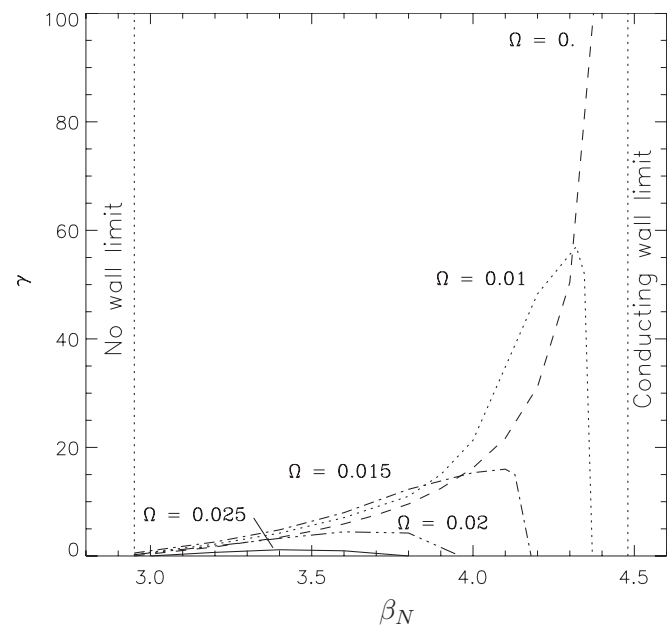

FIG. 6. RWM growth rate normalized to resistive wall time vs beta normal for the strongly reversed shear case. The dashed curve represents the growth rate without plasma rotation and kinetic effects. The dotted ($\Omega = 0.01$), dot-dashed ($\Omega = 0.015$), dot-dot-dashed ($\Omega = 0.02$), and solid ($\Omega = 0.025$) curves are growth rates with plasma rotation and kinetic effects included.
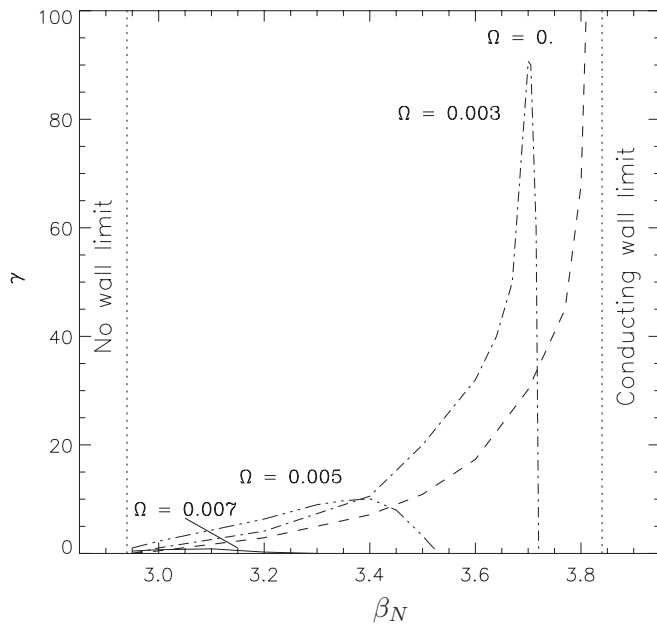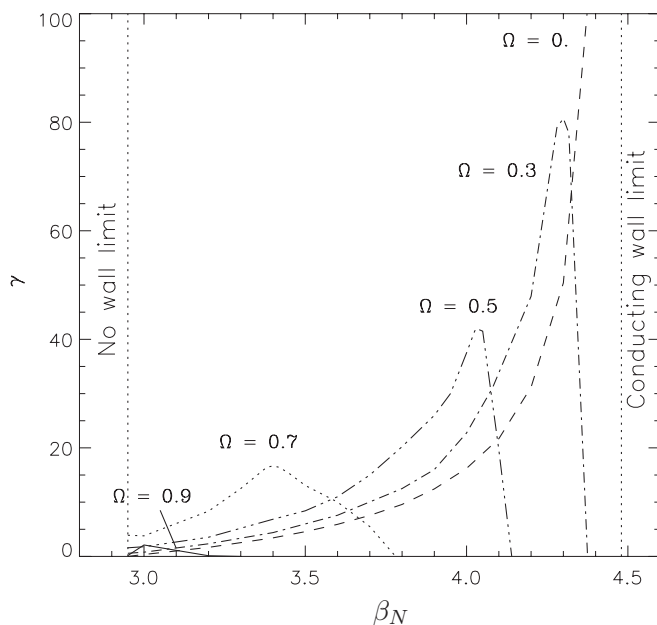
FIG. 7. RWM growth rate normalized to resistive wall time vs beta normal for the weakly reversed shear case (reproduced from data given in Fig. 8 in Ref. 14 with a modified horizontal coordinate). The dashed curve represents the growth rate without plasma rotation and kinetic effects. The dot-dashed (Ω=0.003), dot-dot-dashed (Ω=0.005), and solid (Ω=0.007) curves are growth rates with plasma rotation and kinetic effects included.
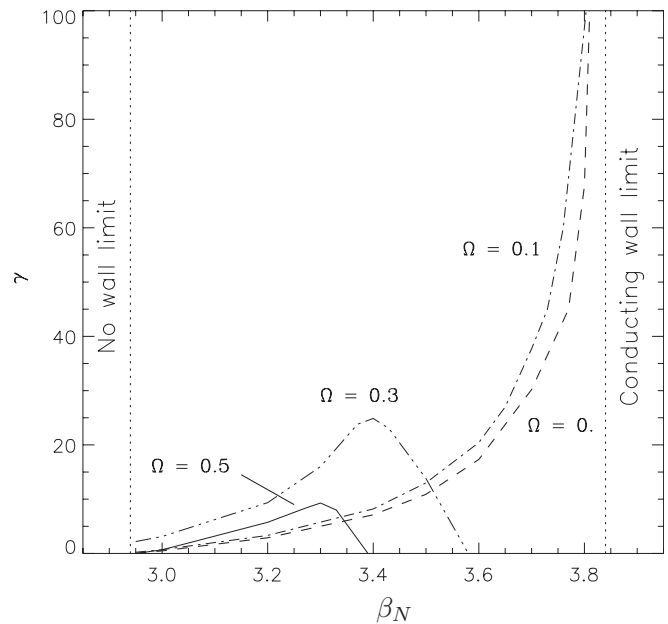

FIG. 9. RWM growth rate normalized to resistive wall time vs beta normal for the weakly reversed shear case. The dashed curve represents the growth rate without plasma rotation and kinetic effects. The dot-dashed (Ω=0.1), dot-dot-dashed (Ω=0.3), and solid (Ω=0.9) curves are growth rates with Alfvén continuum damping taken into account. Full stabilization is found for Ω=0.7. The kinetic resonances are excluded in this figure.

shear case. It appears that the Alfvén and kinetic resonance effects on the reversed shear side are not as strong as those on the normal shear side for stabilization. Possibly this is due to the effect of reversed shear, as noted in the ballooning mode theory.[16] Reversed shear favors stabilization, as com-

pared to the normal shear case. This might make a difference between the resonances on the normal shear side and those on the reversed shear side. Verification of this hypothesis needs further analytical and numerical investigation.

To exclude the kinetic effects, we plot in Figs. 8 and 9 the dependence of the RWM growth rate versus the beta normal, respectively, for strongly and weakly reversed shear cases, with purely Alfvén continuum damping taken into account. Figures 8 and 9 are made using the code in Ref. 6. Therefore, the so-called apparent mass effect has not been taken into account. Using the cylinder estimate, the MHD apparent mass enhancement is about $1+2q^2$. Therefore, the rotation frequency in Figs. 8 and 9 should be scaled down by a factor $1/(1+2q^2)^{1/2}$. Using q=4 for estimate, this factor is about 0.24. From comparison between Figs. 6 and 8 for strongly rotation case and between Figs. 7 and 9 for weakly rotation case, one can see that the rotation stabilization is enhanced significantly when the kinetic effects are taken into account. The kinetic stabilization in the weakly reversed shear case is more significant than in the strongly reversed shear case, as compared to purely Alfvén resonance effect.

IV. DISCUSSION AND CONCLUSIONS

In this paper we investigated the stability of n=1 RWMs in ITER advanced scenarios with strongly reversed shear, in comparison to the weakly reversed shear case that we investigated previously. Our investigation was based on the MHD code AEGIS and the kinetic version AEGIS-K. We developed AEGIS-K based on first principles, namely, the Vlasov and Maxwell equations with suitable ordering scheme. This type of analysis is enabled by our newly derived gyrokinetic formalism in Ref. 8, which recovers MHD in the proper limit

FIG. 8. RWM growth rate normalized to resistive wall time vs beta normal for the strongly reversed shear case. The dashed curve represents the growth rate without plasma rotation and kinetic effects. The dot-dashed (Ω=0.3), dot-dot-dashed (Ω=0.5), dotted (Ω=0.7), and solid (Ω=0.9) curves are growth rates with Alfvén continuum damping taken into account. Full stabilization is found for Ω=1.1. The kinetic resonances are excluded in this figure.

and retrieves missing FLR effects. This feature leads AEGIS-K code to be able to provide a fully kinetic (nonhybrid) and self-consistent (nonperturbative) description of the RWM stability. In the AEGIS-K code, wave-particle resonances, shear Alfvén continuum damping, trapped particle effects, and parallel electric effects are all taken into account. In the calculation reported in the present paper, FLR effects have not been taken into consideration.

We found that, without rotation and kinetic effects taken into account, the strongly reversed shear case is more stable than the weakly reversed shear case. The beta limit with a perfectly conducting wall for the strongly reversed shear case is higher than that for the weakly reversed shear case. With rotation and kinetic effects taken into consideration, the normalized rotation frequency for full rotation stabilization of RWMs in the strongly reversed shear case is $q_0\Omega=0.006$. This is about twice as high as that for the weakly reversed shear case reported in Ref. 14, for which the normalized rotation frequency is $q_0\Omega=0.003$. Nevertheless, it should be noted that the beta value for full stabilization in the strongly reversed shear case ($\beta_N=4.48$) is larger than that for the weakly reversed shear case ($\beta_N=3.84$). Similar to the weakly reversed shear case, we found that the stability window opens first at the conducting wall limit.

In our present investigation, the FLR effects, especially the precessional drift,[7] have been neglected, because we considered only the case of modestly low rotation frequency. Consequently, these results are applicable only to the case with rotation frequency larger than the ion diamagnetic drift frequency, in which case the resonance effects due to the ion precessional drift are excluded. Although the lower range of our parameter domain in Fig. 6 might approach or touch the ion diamagnetic drift frequency, it does not change our demonstration of full rotation stabilization of RWMs above the diamagnetic frequency. In ITER, beam-driven rotation is expected to small, due to a relatively low beam power. Note, however, that there is some uncertainty about the actual value of the rotation in ITER, since so-called spontaneous rotation may occur. The Alcator C-Mod (Ref. 17) experimental results indicate that the spontaneous rotation speed could be about 10% of the ion thermal speed.[18] This rotation frequency is not small. Therefore, the rotation stabilization window found in our paper could be of interest for ITER. The full stabilization rotation frequency for ITER found in this paper is roughly the same as that observed recently in DIII-D (Ref. 19) experiments.[20]

The case with even lower rotation frequency, where the precessional drift resonance occurs,[7,21] is important for future study. The theoretical understanding of the precessional drift resonance effect on RWM stabilization and its experimental validation require more elaborate effort. Theoretically, as we found with our newly developed gyrokinetic theory,[8] FLR effects have been oversimplified in previous studies. Furthermore, the MARS-K code has not taken into account the finite orbit size and the parallel electric field effects, for example.[22] Numerically, Ref. 21 is based on a perturbative method, whereas the nonperturbative hybrid calculations with the MARS-K code show that the perturbative and nonperturbative results differ dramatically.[22] In addition,

the numerical scheme and code validation are also a concern. Due to the complexity of this problem, one could easily lose the MHD benchmark point in the nonperturbative calculations and no longer be able to identify the MHD eigenmode trace as computed from existing MHD codes such as GATO and AEGIS. We plan to use the current results as a starting benchmark point for our subsequent investigations. Comparison of our MHD (Fig. 4) and kinetic (Fig. 5) eigenmodes shows that the MHD trace has been retained. The frequency domain we have here investigated is easier to benchmark (with the use of the Z-function). This is another reason why we are advancing this research slowly and deliberately.

The other important feature of AEGIS-K is its adaptive nature. The eigenfunction in Fig. 5 shows that the radial resolution is a critical issue for kinetic computation. It is challenging for radial-grid-based numerical schemes. In most cases, the radial grid density for the output can run as high as 800 points with packing at the resonance surfaces. The matrix size in the AEGIS-K numerical scheme, however, is determined by the product of the number of poloidal Fourier components and the number of radial integration regions. The latter is approximately the same as the number of mode rational surfaces. Here, we note that, although the number of resonance surfaces doubled due to the splitting of the Alfvén resonance surfaces, the singularity weakens from nearly $1/x^2$ to $1/(x-\Omega)$. Increasing the radial resolution is not accompanied by increasing the matrix size in AEGIS-K. Hence, the AEGIS-K code has the capability to resolve singular layer behavior in the presence of kinetic and shear Alfvén resonances. Usual grid based codes have difficulty meeting this requirement for high- resolution computation.

In the future, we also plan to extend the AEGIS-K code to include the precession drift resonance together with the FLR effects.

ACKNOWLEDGMENTS

[1] K. Ikeda, Nucl. Fusion **47** (2007).
[2] J. P. Freidberg, *Ideal Magnetohydrodynamics* (Clarendon, Oxford, 1987).
[3] T. C. Hender, J. C. Wesley, J. Bialek, A. Bondeson, A. H. Boozer, R. J. Buttery, A. Garofalo, T. P. Goodman, R. S. Granetz, Y. Gribov, O. Gruber, M. Gryaznevich, G. Giruzzi, S. Günter, N. Hayashi, P. Helander, C. C. Hegna, D. F. Howell, D. A. Humphreys, G. T. A. Huysmans, A. W. Hyatt, A. Isayama, S. C. Jardin, Y. Kawano, A. Kellman, C. Kessel, H. R. Koslowski, R. J. La Haye, E. Lazzaro, Y. Q. Liu, V. Lukash, J. Manickam, S. Medvedev, V. Mertens, S. V. Mirnov, Y. Nakamura, G. Navratil, M. Okabayashi, T. Ozeki, R. Paccagnella, G. Pautasso, F. Porcelli, V. D. Pustovitov, V. Riccardo, M. Sato, O. Sauter, M. J. Schaffer, M. Shimada, P. Sonato, E. J. Strait, M. Sugihara, M. Takechi, A. D. Turnbull, E. Westerhof, D. G. Whyte, H. Yoshino, H. Zohm, and ITPA MHD, Disruption and Magnetic Control Topical Group, Nucl. Fusion **47**, S128 (2007).
[4] A. Bondeson and D. J. Ward, Phys. Rev. Lett. **72**, 2709 (1994).
[5] R. Betti and J. P. Freidberg, Phys. Rev. Lett. **74**, 2949 (1995).
[6] L. J. Zheng, M. Kotschenreuther, and M. Chu, Phys. Rev. Lett. **95**, 255003 (2005).
[7] B. Hu and R. Betti, Phys. Rev. Lett. **93**, 105002 (2004).
[8] L. J. Zheng, M. T. Kotschenreuther, and J. W. Van Dam, Phys. Plasmas **14**, 072505 (2007).

[9]L. J. Zheng and M. Kotschenreuther, J. Comput. Phys. **211**, 748 (2006).

[10]L. J. Zheng, M. T. Kotschenreuther, and J. W. Van Dam, "AEGIS-K code for linear kinetic analysis of toroidally axisymmetric plasma stability," J. Comput. Phys. (to be published).

[11]L. C. Bernard, F. J. Helton, and R. W. Moore, Comput. Phys. Commun. **24**, 377 (1981).

[12]M. N. Rosenbluth and N. Rostoker, Phys. Fluids **2**, 23 (1959).

[13]L.-J. Zheng, M. S. Chu, and L. Chen, Phys. Plasmas **6**, 1217 (1999).

[14]L. J. Zheng, M. T. Kotschenreuther, and J. W. Van Dam, Nucl. Fusion **49**, 075021 (2009).

[15]R. L. Miller and J. W. Van Dam, Nucl. Fusion **27**, 2101 (1987).

[16]X. Llobet, H. L. Berk, and M. N. Rosenbluth, Phys. Fluids **30**, 2750 (1987).

[17]M. Greenwald, D. Andelin, N. Basse, S. Bernabei, P. Bonoli, B. Bšse, C. Boswell, R. Bravenec, B. Carreras, I. Cziegler, E. Edlund, D. Ernst, C. Fasoli, M. Ferrara, C. Fiore, R. Granetz, O. Grulke, T. Hender, J. Hosea, D. H. Howell, A. Hubbard, J. Hughes, I. Hutchinson, A. Ince-Cushman, J. Irby, B. LaBombard, R. LaHaye, L. Lin, Y. Lin, B. Lipschultz, J. Liptac, S. Lisgo, A. Lynn, E. Marmar, K. Marr, D. R. Mikkelsen, R. McDermott, D. Mossessian, A. Parisot, R. Parker, C. Phillips, P. Phillips, M. Porkolab, M. Redi, J. Rice, W. Rowan, M. Sampsell, G. Schilling, S. Scott, J. T. Scoville, N. Smick, J. Snipes, P. Stangeby, V. Tang, J. Terry, M. Ulrickson, G. Wallace, D. Whyte, J. Wilson, J. Wright, S. Wolfe, S. Wukitch, B. Youngblood, H. Yuh, K. Zhurovich, and S. Zweben, Nucl. Fusion **45**, S109 (2005).

[18]J. E. Rice, M. Greenwald, I. H. Hutchinson, E. S. Marmar, Y. Takase, S. M. Wolfe, and F. Bombarda, Nucl. Fusion **38**, 75 (1998).

[19]J. L. Luxon, Nucl. Fusion **42**, 614 (2002).

[20]A. M. Garofalo, W. M. Solomon, M. Lanctot, K. H. Burrell, J. C. DeBoo, J. S. deGrassie, G. L. Jackson, J.-K. Park, H. Reimerdes, M. J. Schaffer, and E. J. Strait, Phys. Plasmas **16**, 056119 (2009).

[21]B. Hu, R. Betti, and J. Manickam, Phys. Plasmas **12**, 057301 (2005).

[22]Y. Liu, M. S. Chu, I. T. Chapman, and T. C. Hender, Phys. Plasmas **15**, 112503 (2008).